Planetary and Space Science 101 (2014) 77–88

Contents lists available at ScienceDirect

Planetary and Space Science

journal homepage: www.elsevier.com/locate/pss

# How to process radio occultation data: 1. From time series of frequency residuals to vertical profiles of atmospheric and ionospheric properties

Paul Withers [a,b,*], L. Moore [b], K. Cahoy [c], I. Beerer [c]

[a] Department of Astronomy, Boston University, 725 Commonwealth Avenue, Boston, MA 02215, USA
[b] Center for Space Physics, Boston University, 725 Commonwealth Avenue, Boston, MA 02215, USA
[c] Department of Aeronautics and Astronautics, MIT, 77 Massachusetts Avenue, Cambridge, MA 02139, USA

ARTICLE INFO

*Article history:*
Received 4 January 2014
Received in revised form
17 June 2014
Accepted 23 June 2014
Available online 2 July 2014

*Keywords:*
Radio occultation
Ionosphere
Atmosphere
Data processing

ABSTRACT

Expertise in processing radio occultation observations, which provide vertical profiles of atmospheric and ionospheric properties from measurements of the frequency of radio signals, is not widespread amongst the planetary science community. In order to increase the population of radio occultation processing experts, which will have positive consequences for this field, here we provide detailed instructions for one critical aspect of radio occultation data processing: how to obtain a series of bending angles as a function of the ray impact parameter from a time series of frequency residuals. As developed, this tool is valid only for one-way, single frequency occultations at spherically symmetric objects, and is thus not immediately applicable to either two-way occultations, such as those of Mars Express, or occultations at oblate objects, such as Jupiter or Saturn. This tool is demonstrated successfully on frequency residuals from a Mars Global Surveyor occultation at Mars, and the resultant set of bending angles and impact parameters are used to obtain vertical profiles of ionospheric electron density, neutral atmospheric number density, mass density, pressure, and temperature via the usual Abel transform. The root-mean-square difference between electron densities in the ionospheric profile derived herein and archived electron densities is $7 \times 10^8$ m$^{-3}$. At the lowest altitudes, temperatures in the neutral atmospheric profile derived herein differ from archived neutral temperatures by less than 0.1 K. Software programs that implement these procedures accompany this paper and may be used to extract scientifically useful data products from lower-level data sets.



## 1. Introduction

Radio occultation investigations have been commonplace on planetary science flyby and orbital missions since Mariner 4 reached Mars in 1965 (Kliore et al., 1965), with dozens of spacecraft performing radio occultations at many planets, satellites, and a comet (Withers, 2010). The application of radio occultation investigations to planetary science has been described previously by several authors (e.g. Phinney and Anderson, 1968; Fjeldbo et al., 1971; Yakovlev, 2002; Kliore et al., 2004; Withers, 2010). These investigations transmit a radio signal such that it passes close to a solar system object (the "target object") during its journey from the transmitter to the receiver. Refraction of the radio signal in the neutral gas and ionospheric plasma around the target object affects the frequency of the radio signal. Vertical profiles of the number density of neutral gas and the electron density of ionospheric plasma can be obtained from time series measurements of the received radio frequency. Corresponding profiles of neutral mass density, pressure, and temperature can also be obtained. The resultant neutral atmospheric profiles offer better vertical resolution (sub-km) than most other techniques and are unaffected by instrument calibration issues. They are also referenced to an absolute altitude scale, unlike the pressure levels that are common to many infrared instruments, which provides deeper context for studies of atmospheric dynamics. In addition, compared to data sets from many other instruments, they have high accuracy at relatively high pressures, which enhances studies of tropospheric climate and, on objects whose surface pressure is not much greater than Earth's, atmosphere–surface interactions. Radio occultation investigations are even more valuable for planetary ionospheric studies than for planetary atmospheric studies—indeed, they have provided almost all measurements of planetary ionospheres.

However, the expertise necessary to obtain useful information about planetary environments from the recorded frequency measurements has not been widely disseminated across the scientific community in the 50 years since these skills were first developed.

* Corresponding author at: Center for Space Physics, Boston University, 725 Commonwealth Avenue, Boston, MA 02215, USA.
*E-mail address:* withers@bu.edu (P. Withers).

http://dx.doi.org/10.1016/j.pss.2014.06.011
0032-0633/

With one exception, merely two institutions, the NASA Jet Propulsion Laboratory (JPL) and Stanford, have provided the Principal Investigators or Team Leaders for every NASA planetary radio occultation investigation (see list of investigations and personnel at http://nssdc.gsfc.nasa.gov/planetary/ for each mission). The exception occurred when Dick French of Wellesley College replaced Arv Kliore of JPL as Principal Investigator of the Cassini Radio Science Subsystem some time after completion of Cassini's nominal mission. These two institutions have also provided most of the team members with instrumentation, operations, or data processing expertise (as opposed to scientific analysis of derived atmospheric and ionospheric properties). This localization of expertise was identified as a potential concern in the 1970s when Nicholson and Muhleman (1978) stated that "such an important experiment should be subject to independent confirmation, both to determine the reproducibility of the results and to check for systematic errors." They successfully reproduced the reported results of the Mariner 10 radio occultation investigation. Expertise also exists in Europe, where groups from Cologne and Munich lead radio science investigations on Rosetta, Mars Express, and Venus Express (Pätzold et al., 2004, 2007; Häusler et al., 2006); Japan, where the Sakigake, Nozomi, Selene, and Akatsuki spacecraft carried radio occultation investigations (Oyama et al., 2001; Noguchi et al., 2002; Imamura et al., 2011, 2012); and China (Hu et al., 2010). Several groups also possess related expertise concerning radio occultations of Earth's atmosphere and ionosphere (e.g. Kursinski et al., 1997, 2000; Anthes et al., 2008).

Consequently, radio occultation investigations are often viewed by the planetary science community as an esoteric speciality. Hands-on analysis of all radio occultation data products that precede the final vertical profiles of neutral atmospheric and ionospheric properties has been conducted by only a small subset of those using these final products. It is clearly detrimental to the advancement of planetary science for the vast majority of the users of these data sets to have such limited awareness of the preceding data processing steps. For instance, such users are hard-pressed to critically evaluate whether an unusual feature in the final data products is an exciting scientific discovery or an instrumental glitch. Another consequence is that atmospheric and ionospheric profiles that were not comprehensively archived by the original investigators are effectively lost, since barely any scientists interested in analyzing these profiles have the skills necessary to recover them. This is not merely a hypothetical concern: the atmospheric and ionospheric profiles acquired by missions as significant as Pioneer Venus Orbiter, the Voyagers, and the Viking Orbiters are not archived. Images of some of these profiles may be present, in cramped and cropped formats, in published articles, but today's scientists are unable to work meaningfully with these profiles. If the size of the community capable of obtaining such profiles from raw radio occultation data were to increase, then some of these past data sets could be regenerated and the chances of current and future data sets suffering a similar fate would diminish.

Our aim in this paper is to make this arcane skill more readily accessible to the broader scientific community. Although the theory of how to process radio occultation data has been presented in several publications, it is exceedingly challenging to create a functional radio occultation processing tool from the scientific literature without mentoring from an expert. Many issues important for practical implementation are stated either implicitly or not at all. Here we describe how to implement one of the key steps in the processing of radio occultation data: the determination of vertical profiles of atmospheric properties from time series of "frequency residuals". As will be explained in more detail in Section 3, the frequency residual is the difference between the frequency of the received radio signal and the frequency it would have had in the absence of refraction in the atmosphere and ionosphere of the solar system object that is the target of the occultation. The frequency residual is intimately associated with the number densities of neutral gas and ionospheric plasma around the target object. The software programs that were developed in the course of writing this paper accompany this publication, and we hope these programs in the IDL programming language will encourage many readers to work more closely with radio occultation data sets.

There are many types of radio occultation experiments and here we focus on the simplest example: a one-way, single frequency downlink experiment with a transmitter that has a stable frequency source and a target object whose atmosphere and ionosphere can be assumed to be spherically symmetric. Mars Global Surveyor is representative of this type of radio occultation experiment. We focus on this simple type because it offers the clearest possible framework for establishing and illustrating the practical principles of a radio occultation experiment. We discuss the numerous limitations that arise from this decision in Section 5. It is hoped that this will be the first of a series of papers concerning how to process radio occultation data in which the future papers will present more sophisticated tools developed from the present work that are suitable for more complex radio occultation experiments.

Detailed knowledge of the positions and velocities of solar system objects, both natural and artificial, as functions of time is required for the interpretation of radio occultation observations. The JPL SPICE system provides a remarkably straightforward, yet powerful, tool for obtaining and manipulating such information (http://naif.jpl.nasa.gov). Our software makes extensive use of SPICE and it is painful to imagine how radio occultation data processing would be accomplished without a tool like SPICE.

Section 2 explains why the angle by which a radio ray is bent is useful. Section 3 describes how to derive vertical profiles of ray bending angles from time series of frequency residuals. It presents the basic requirements (Section 3.1), explains how the relativistic Doppler shift alters the radio frequency (Section 3.2), introduces the concept of the frequency residual (Section 3.3), and links the frequency residual to the bending angle (Sections 3.4–3.7). Section 4 applies this method to a sample of Mars Global Surveyor data from Mars, including the transformation of bending angles into vertical profiles of refractive index, ionospheric electron density, neutral density, pressure, and temperature. These results are validated against archived results. Section 5 discusses the many limitations of our method, which is less sophisticated than the state-of-the-art tools used by active flight missions. Section 6 presents the conclusions of this work.

## 2. Why bending angles are useful

The objective of a radio occultation is to obtain scientifically useful information about the environment through which a radio signal has propagated by analysis of properties of that radio signal. The primary environmental property that is usually determined is the refractive index. In geometric optics, the direction of propagation of a ray depends on the refractive index, $n$, as follows (Born and Wolf, 1959):

$$\frac{d}{dl}(n\underline{\hat{l}}) = \underline{\nabla} n \tag{1}$$

Here unit vector $\underline{\hat{l}}$ is the direction of propagation of the ray. Consequently, the path of a radio ray bends as it passes through an atmosphere or ionosphere, except for the unlikely case of radio transmission through a medium in which the gradient of refractive index is parallel to the direction of propagation. The total angle by

which a radio ray is bent during its passage through an atmosphere and/or ionosphere depends on the refractivity of the environment through which it passes. Under certain assumptions, the dependence of the refractive index on radial distance can be obtained from the dependence of bending angle on the impact parameter. In turn, neutral and plasma densities can be found from the refractive index. Hence radial profiles of neutral and plasma densities can be obtained from the dependence of bending angle on impact parameter. Therefore it would be useful in a radio occultation to determine the bending angle of radio signals as a function of impact parameter. However, the bending angle itself is not directly observable. Hence we outline how changes in the frequency of a radio signal, which are readily observable, are related to bending angle. That information will be sufficient for the determination of radial profiles of neutral and plasma densities, quantities which are scientifically useful.

## 3. From frequency residuals to bending angles

### 3.1. Basic requirements

Here we describe how to determine the bending experienced by a radio signal given information about the frequency of the received radio signal. Our objective is to obtain a series of bending angles as a function of impact parameter, from which neutral and plasma densities can eventually be determined. We describe the occultation geometry, how the relativistic Doppler shift alters the radio frequency, and how refractive bending of the ray affects the frequency.

Fig. 1 shows the canonical description of the geometry of a radio occultation observation, based on Figure 20 of Fjeldbo et al. (1971). The discussion in Section 3 builds upon the themes and approaches introduced by Fjeldbo et al. (1971), but with the addition of relativistic corrections and explicit instructions on how to calculate the necessary quantities. We use different symbols from those in Fjeldbo et al. (1971) in order to better emphasize aspects of our technique. Table 1 provides a conversion table for these symbols.

We use $\underline{x}_i$ to represent the vector position of location $i$, where $i$ is $A$ (transmitter), $B$ (receiver), $P$ (target object), $O$ (defined below),

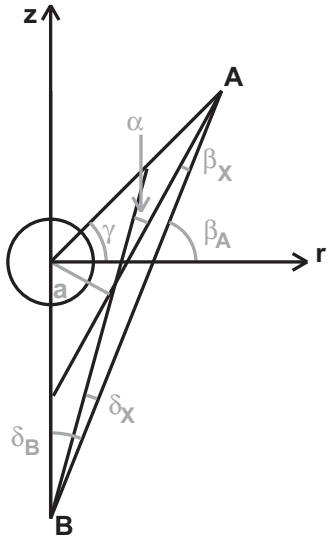


**Fig. 1.** Geometry for an occultation involving transmitter $A$, receiver $B$, and target object $P$ at the origin. The remaining symbols are defined in the text. The position $\underline{x}_X$ lies at the intersection of the two asymptotes to the ray path and the position $\underline{x}_O$ lies close to $\underline{x}_X$.

**Table 1**
Conversions between symbols used in this work and in Fjeldbo et al. (1971).

| Fjeldbo et al. (1971) | This work |
|---|---|
| $f_s$ | $f_A(t_A)$ |
| $r_t$[a] | $r_B(t_B)$ |
| $z_t$ | $z_B(t_B)$ |
| $r_s$ | $r_A(t_A)$ |
| $z_s$ | $z_A(t_A)$ |
| $\nu_{rs}$ | $\nu r_A(t_A)$ |
| $\nu_{zs}$ | $\nu z_A(t_A)$ |
| $\nu_{rt}$ | $\nu r_B(t_B)$ |
| $\nu_{zt}$ | $\nu z_B(t_B)$ |
| $\beta_e$ | $\beta_A$ |
| $\beta_r$ | $\beta_X$ |
| $\delta_s$ | $\delta_B$ |
| $\delta_r$ | $\delta_X$ |
| $\gamma$ | $\gamma$ |

[a] Symbol not explicitly used in Fjeldbo et al. (1971) since its value is by definition zero.

or $X$ (defined below). In Fig. 1, the radio signal is transmitted from $\underline{x}_A$ at time $t_A$ and received at $\underline{x}_B$ at time $t_B$. Instead of proceeding directly along the straight line path between the position of the transmitter $A$ at time $t_A$ and the position of the receiver $B$ at time $t_B$, it moves initially away from the position of the transmitter $A$ at time $t_A$ in a straight line at some angle to the anticipated trajectory. It passes through the atmosphere and ionosphere of the target object $P$ and emerges on a final straight line path towards the position of the receiver $B$ at time $t_B$. Refraction in the atmosphere and ionosphere of the target object has changed the direction of propagation of the radio signal. We call the initial and final straight line paths the two asymptotes of the ray path. The point of closest approach of the radio signal transmitted at time $t_A$ to the target object $P$ is $\underline{x}_O$, the time at which this radio signal is at this position is $t_O$, and the two asymptotes of this ray path intersect at position $\underline{x}_X$. Note that $\underline{x}_O \neq \underline{x}_X$.

Fig. 1 shows the position of the centers of mass of the transmitter $A$ at time $t_A$, the receiver $B$ at time $t_B$, and the target object $P$ at time $t_O$. The conceptual differences between these three times are particularly important. For instance, the position and velocity of the receiver $B$ may change significantly between the time the radio signal is transmitted ($t_A$) and the time it is received ($t_B$). In calculations of the Doppler shift in the radio signal transmitted at time $t_A$, the state of the receiver $B$ at time $t_A$ is irrelevant; its state at time $t_B$ is what matters. Here we first assume that $t_A$, $t_B$, and $t_O$ are known somehow. Section 3.7 outlines how to determine $t_A$ and $t_O$ given $t_B$.

Errors in time definitions can hence have significant impact on the results of a radio occultation. Every quantity that will be defined in Section 3, whether a position, velocity, angle, or frequency, is associated with a particular time. In some cases, such as the positions of objects, the associated time is fairly obvious, but in other cases, such as distances between objects or angles between vectors, the associated time might be less obvious.

The coordinate frame shown in Fig. 1 is defined as follows. The origin is at $\underline{x}_P(t_O)$. The unit vectors $\hat{\underline{r}}(t_O)$, $\hat{\underline{z}}(t_O)$, and $\hat{\underline{n}}(t_O)$ satisfy

$$\hat{\underline{z}}(t_O) = \frac{(\underline{x}_P(t_O) - \underline{x}_B(t_B))}{|(\underline{x}_P(t_O) - \underline{x}_B(t_B))|}$$

$$\hat{\underline{n}}(t_O) = \frac{(\underline{x}_A(t_A) - \underline{x}_P(t_O))}{|(\underline{x}_A(t_A) - \underline{x}_P(t_O))|} \times \hat{\underline{z}}$$

$$\hat{\underline{r}}(t_O) = \hat{\underline{z}} \times \hat{\underline{n}} \qquad (2)$$

The unit vector $\hat{\underline{n}}(t_O)$, which is not shown in Fig. 1, points upwards out of the page. The definition of $\hat{\underline{z}}(t_O)$ ensures that the $r$-component of $\underline{x}_B(t_B)$ is zero and the $z$-component of $\underline{x}_B(t_B)$ is

negative, while the definition of $\hat{\underline{r}}(t_O)$ ensures that the $r$-component of $\underline{x}_A(t_A)$ is positive. Assuming that this frame is used when an occultation occurs, the $z$-component of $\underline{x}_A(t_A)$ must be positive as well. Many other possible coordinate frames exist; the rationale for emphasizing this particular coordinate frame is provided in Section 3.4.

### 3.2. Doppler shift—effects of special and general relativity

According to Eq. (5.2.4) of Soffel (1989) and Eq. (7) of Häusler et al. (2007), the relationship between a transmitted frequency $f_A$ and a received frequency $f_B$ is

$$\frac{f_B(t_B)}{f_A(t_A)}=\frac{1-\frac{\underline{v}_B(t_B)\cdot\hat{\underline{n}}_B(t_B)}{c}-\frac{U_B(t_B)}{c^2}+\frac{v_B(t_B)^2}{2c^2}}{1-\frac{\underline{v}_A(t_A)\cdot\hat{\underline{n}}_A(t_A)}{c}-\frac{U_A(t_A)}{c^2}+\frac{v_A(t_A)^2}{2c^2}} \tag{3}$$

Here $\underline{v}_B$ is the velocity of the receiver, $\hat{\underline{n}}_B$ is the unit vector along which the radio wave propagates into the receiver, $U_B$ is the gravitational potential at the receiver, $\underline{v}_A$ is the velocity of the transmitter, $\hat{\underline{n}}_A$ is the unit vector along which the radio wave propagates away from the transmitter, and $U_A$ is the gravitational potential at the transmitter. This expression is accurate to order $(v/c)^2$. Note that all the quantities in this equation must be referenced to the same inertial frame.

### 3.3. Introduction of the frequency residual

Suppose there is no refraction at the target object $P$. In this case, the radio signal travels directly from the transmitter to the receiver and the unit vectors $\hat{\underline{n}}_B(t_B)$ and $\hat{\underline{n}}_A(t_A)$ are equal. We label these as the "direct" unit vectors $\hat{\underline{n}}_{B,Direct}(t_B)$ and $\hat{\underline{n}}_{A,Direct}(t_A)$. The received radio frequency is $f_{B,Direct}(t_B)$. If refraction of the radio signal occurs at the target object, as illustrated in Fig. 1, then these two unit vectors are different and we label these as the "occultation" unit vectors $\hat{\underline{n}}_{B,Occ}(t_B)$ and $\hat{\underline{n}}_{A,Occ}(t_A)$. Now the received radio frequency is $f_{B,Occ}(t_B)$.

The difference between $f_{B,Occ}(t_B)$ and $f_{B,Direct}(t_B)$ is known as the frequency residual, $\Delta f(t_B)$. It can be found from the measured $f_{B,Occ}(t_B)$ and the theoretically calculated $f_{B,Direct}(t_B)$. It can also be related to the refractive properties of the target object:

$$\frac{\Delta f(t_B)}{f_A(t_A)}=\left(\frac{1-\frac{\underline{v}_B(t_B)\cdot\hat{\underline{n}}_{B,Occ}(t_B)}{c}-\frac{U_B(t_B)}{c^2}+\frac{v_B(t_B)^2}{2c^2}}{1-\frac{\underline{v}_A(t_A)\cdot\hat{\underline{n}}_{A,Occ}(t_A)}{c}-\frac{U_A(t_A)}{c^2}+\frac{v_A(t_A)^2}{2c^2}}\right)-\left(\frac{1-\frac{\underline{v}_B(t_B)\cdot\hat{\underline{n}}_{B,Direct}(t_B)}{c}-\frac{U_B(t_B)}{c^2}+\frac{v_B(t_B)^2}{2c^2}}{1-\frac{\underline{v}_A(t_A)\cdot\hat{\underline{n}}_{A,Direct}(t_A)}{c}-\frac{U_A(t_A)}{c^2}+\frac{v_A(t_A)^2}{2c^2}}\right) \tag{4}$$

Though the relativistic Eq. (4) is used throughout this work for completeness, the Appendix describes the non-relativistic version of Eq. (4). The non-relativistic version provides an uncluttered perspective on the major factors affecting the frequency residual, leading to the counter-intuitive result that the frequency residual is dominated by the velocity component perpendicular to, not parallel to, the line of sight. In the Mars Global Surveyor example that will be introduced in Section 4, the ratios of the relativistic $(v/c)^2$ and $U/c^2$ terms to the non-relativistic $v/c$ term are both on the order of 1 part in $10^5$ and relativistic effects are therefore insignificant. This is not always the case.

### 3.4. Assumption of spherical symmetry

In order to proceed further with this expression, we must make a significant decision concerning the frame in which we shall work. In order for a particular radio ray to remain confined to the plane outlined in Fig. 1, which greatly simplifies analysis, the refractive environment at the target object $P$ must be spherically symmetric *as encountered by the ray*. That requires that our frame be moving with the target object $P$. Consequently, $\underline{v}_A(t_A)$ equals $\dot{\underline{x}}_A(t_A)-\dot{\underline{x}}_P(t_O)$, where an overdot indicates a derivative with respect to time, and $\underline{v}_B(t_B)$ equals $\dot{\underline{x}}_B(t_B)-\dot{\underline{x}}_P(t_O)$. We further define $vr_A(t_A)$ as the $r$-component of $\underline{v}_A(t_A)$, which equals $\underline{v}_A(t_A)\cdot\hat{\underline{r}}(t_O)$ and define $vz_A(t_A)$, $vr_B(t_B)$, and $vz_B(t_B)$ similarly.

The assumption of spherical symmetry introduces limitations that are addressed further in Section 5. One of the limitations is that our results will not be applied to oblate planets, such as Jupiter, Saturn, Uranus, and Neptune. In such instances, gradients of refractivity exist perpendicular to the $r-z$ plane in Fig. 1 that contains the transmitter, receiver, and target object and thus the radio signal will travel outside this plane (as required by Eq. (1)).

### 3.5. Angles

We next define four angles that are useful for describing the unit vectors in Eq. (4): $\delta_B$, $\beta_A$, $\delta_X$, and $\beta_X$.

The angle $\delta_B$ is defined by

$$\tan\,\delta_B=\frac{(r_A(t_A)-r_B(t_B))}{(z_A(t_A)-z_B(t_B))} \tag{5}$$

The angle $\beta_A$ is defined by

$$\beta_A+\delta_B=90^\circ \tag{6}$$

Note that the definition of the coordinate system requires that $0^\circ<\delta_B<90^\circ$ and $0^\circ<\beta_A<90^\circ$ during an occultation. Hence $\cos\,\beta_A=\sin\,\delta_B$ and $\sin\,\beta_A=\cos\,\delta_B$.

The angle $\delta_X$ is defined by

$$\tan(\delta_B-\delta_X)=\frac{(r_X(t_O)-r_B(t_B))}{(z_X(t_O)-z_B(t_B))} \tag{7}$$

The angle $\beta_X$ is defined by

$$\tan(\beta_A-\beta_X)=\frac{(r_A(t_A)-r_X(t_O))}{(z_A(t_A)-z_X(t_O))} \tag{8}$$

With these definitions, we have

$$-\hat{\underline{n}}_{B,Direct}(t_B)=\hat{\underline{r}}(t_O)\sin\,\delta_B+\hat{\underline{z}}(t_O)\cos\,\delta_B \tag{9}$$

$$-\hat{\underline{n}}_{B,Occ}(t_B)=\hat{\underline{r}}(t_O)\sin(\delta_B-\delta_X)+\hat{\underline{z}}(t_O)\cos(\delta_B-\delta_X) \tag{10}$$

$$-\hat{\underline{n}}_{A,Direct}(t_A)=\hat{\underline{r}}(t_O)\cos\,\beta_A+\hat{\underline{z}}(t_O)\sin\,\beta_A \tag{11}$$

$$-\hat{\underline{n}}_{A,Occ}(t_A)=\hat{\underline{r}}(t_O)\cos(\beta_A-\beta_X)+\hat{\underline{z}}(t_O)\sin(\beta_A-\beta_X) \tag{12}$$

### 3.6. Solution for unknown angles

Thus, dropping the explicit time references for clarity, Eq. (4) becomes

$$\frac{\Delta f}{f_A}=\left(\frac{1+\frac{vr_B\,\sin(\delta_B-\delta_X)+vz_B\,\cos(\delta_B-\delta_X)}{c}-\frac{U_B}{c^2}+\frac{v_B^2}{2c^2}}{1+\frac{vr_A\,\cos(\beta_A-\beta_X)+vz_A\,\sin(\beta_A-\beta_X)}{c}-\frac{U_A}{c^2}+\frac{v_A^2}{2c^2}}\right)-\left(\frac{1+\frac{vr_B\,\sin\,\delta_B+vz_B\,\cos\,\delta_B}{c}-\frac{U_B}{c^2}+\frac{v_B^2}{2c^2}}{1+\frac{vr_A\,\cos\,\beta_A+vz_A\,\sin\,\beta_A}{c}-\frac{U_A}{c^2}+\frac{v_A^2}{2c^2}}\right) \tag{13}$$

With two exceptions, all the variables in Eq. (13) are either known at the appropriate times ($\Delta f$, $f_A$, $c$, $U_A$, $U_B$) or can be obtained from trajectory information for the receiver $A$, transmitter $B$, and target object $P$ (the remaining variables). The two exceptions are the angles $\beta_X$ and $\delta_X$.

Thankfully, the two angles $\beta_X$ and $\delta_X$ can also be related to the geometry of the occultation. Since the spatial distribution of refractivity around the target object $P$ is spherically symmetric, then the closest approaches of the two asymptotes to the center of mass of the target object $P$ are identical. This follows from the requirement that the ray path be invariant under time reversal. We label this closest approach distance as the impact parameter, $a$, which satisfies the following two equations:

$$a(t_O) = -z_B(t_B)\sin(\delta_B - \delta_X) \tag{14}$$

$$a(t_O) = (r_A^2(t_A) + z_A^2(t_A))^{1/2}\ \sin(\beta_A - \beta_X - \gamma) \tag{15}$$

where $\gamma$ satisfies

$$\tan\ \gamma = \frac{z_A(t_A)}{r_A(t_A)} \tag{16}$$

Note that the impact parameter, $a(t_O)$, does not equal $|\underline{x}_P(t_O) - \underline{x}_X(t_O)|$, as can be seen in Fig. 1 and Fjeldbo et al. (1971). If the impact parameter $a(t_O)$ is eliminated from Eqs. (14)–(15), then we have

$$-z_B(t_B)\sin(\delta_B - \delta_X) = (r_A^2(t_A) + z_A^2(t_A))^{1/2}\ \sin(\beta_A - \beta_X - \gamma) \tag{17}$$

Again, with the exception of the angles $\beta_X$ and $\delta_X$, all the variables in Eq. (17) can be obtained from trajectory information for the receiver $A$, transmitter $B$, and target object $P$. We have two equations (Eqs. (13) and (17)) and two unknowns ($\beta_X$ and $\delta_X$). These two equations can be solved for the two unknowns, providing the values of $\beta_X$ and $\delta_X$ for an individual radio ray. Note that a useful numerical technique for solving the non-relativistic versions of these two equations for the angles $\beta_X$ and $\delta_X$ was introduced by Fjeldbo et al. (1971). After solutions for $\beta_X$ and $\delta_X$ are obtained for all rays recorded at the receiver, the values of $\beta_X$ and $\delta_X$ are known as functions of time during the occultation. From these, the total angle of refraction, $\alpha$, and the impact parameter, $a$, can be obtained as functions of time:

$$\alpha = \beta_X + \delta_X \tag{18}$$

$$a(t_O) = (r_A^2(t_A) + z_A^2(t_A))^{1/2}\ \sin(\beta_A - \beta_X - \gamma) \tag{19}$$

That achieves the objective of this section, which was to obtain a series of bending angles as a function of impact parameter, from which neutral and plasma densities can then be determined.

### 3.7. Determination of times

In order for the technique outlined in Section 3 to be implemented, the times $t_A$, $t_O$, and $t_B$ must be known. In principle, they and all quantities in Eq. (4) should be referenced to the same inertial frame. That is, UTC times at the transmitter $A$, receiver $B$, and the target object $P$ should be corrected for relativistic effects. We neglect that step in this analysis, since the results of an example based on Mars Global Surveyor data are acceptable without it.

Since we assume the existence of a time series of frequency residuals, the time of receipt, $t_B$, must be known. Since the transmitter $A$ and the receiver $B$ are both solar system objects, whether natural or artificial, following deterministic trajectories, the time of transmission, $t_A$, can be found from $|\underline{x}_A(t_A) - \underline{x}_B(t_B)| = c(t_B - t_A)$. Existing tools in SPICE can perform this calculation straightforwardly. However, the occultation point, $\underline{x}_O$, does not obey Newton's laws of motion and its trajectory is not known a priori. Accordingly, an iterative approach can be used to find $t_O$. The following assumes that the target object $P$ is closer to the transmitter $A$ than to the receiver $B$. Extension to the alternative case is trivial. Assume first that $t_O$ equals the known $t_A$. Construct the direct, unrefracted ray path from the transmitter $A$ at time $t_A$ to the receiver $B$ at time $t_B$ and find the point along this line at which the separation between the line and the position of the target object $P$ at time $t_0$ is minimum. Call this point the "pseudo-occultation point" and find the travel time $\Delta t$ between the "pseudo-occultation point" and the position of transmitter $A$ at $t_A$. The sum $t_A + \Delta t$ can be used as the new value of $t_O$ and this iterative process can be repeated until acceptable convergence is achieved. Once the entire occultation data set has been processed and the actual set of ray paths determined, then it can be verified that each "pseudo-occultation point" is sufficiently close to its corresponding true occultation point for the inferred set of occultation times $t_0$ to be deemed accurate.

## 4. Demonstration using MGS data

### 4.1. Preamble

The techniques developed in Section 3 were validated on a Mars Global Surveyor (MGS) occultation at Mars. Here MGS is the transmitter, Earth the receiver, and Mars the target object. Dave Hinson of the MGS radio science team supplied us with time series of frequency residuals for an ingress occultation that occurred on 27 December 1998, during Phase 2 of MGS aerobraking (Withers et al., 2003a), at a UTC time near 13:00. Their temporal resolution is 0.4 s. The occultation geometry is shown in Fig. 2.

We will compare our final results to the profiles of neutral atmospheric properties and ionospheric electron densities that were obtained by the MGS team from this occultation and that have been archived at the Planetary Data System (PDS), where they bear the identifier 8361M48A. These archived profiles were acquired from http://atmos.nmsu.edu/PDS/data/mors_1101/tps/1998_358/ and http://atmos.nmsu.edu/PDS/data/mors_1102/eds/1998_358/. The SPICE kernels used were pck00009.tpc (rotational states of solar system objects), de414.bsp (trajectories of solar system objects), naif0009.tls (record of leap seconds), mgs_ab2.bsp (MGS trajectory), earthstns_fx_050714.bsp, and earth_topo_050714.tf, and earth_720101_070426.bpc (trajectories of Deep Space

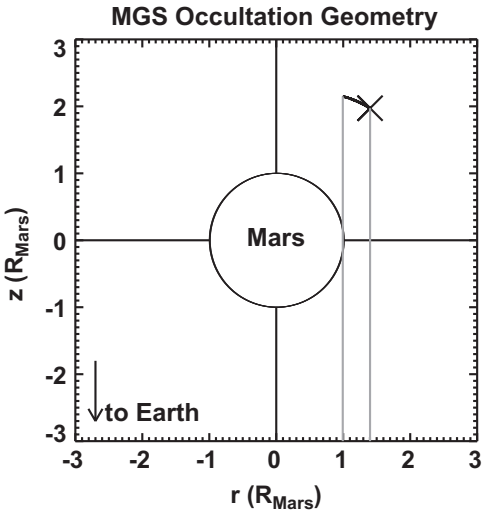


**Fig. 2.** Geometry for MGS occultation 8361M48A using the frame introduced in Fig. 1. The $X$ indicates the initial position of MGS and the adjacent curved black line indicates the path of MGS during the occultation, confirming that this is an ingress occultation. This line terminates at the point where MGS passed behind the solid surface of Mars as viewed from Earth. The two vertical grey lines indicate the ray paths between MGS and Earth at the start and end of the occultation. An arrow points towards Earth, whose $r$-coordinate is zero and whose $z$-coordinate is negative and very large.

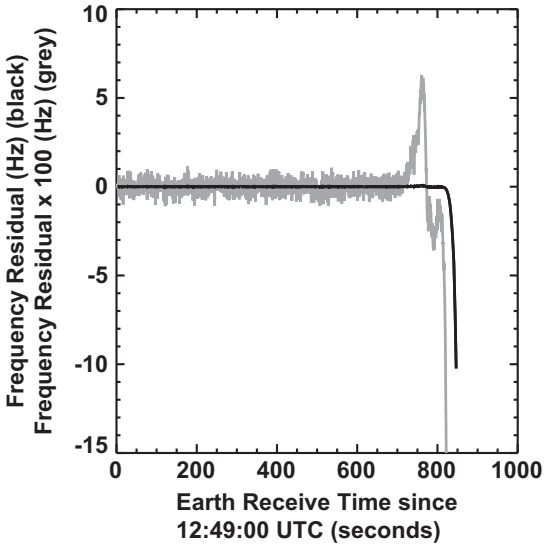


**Fig. 3.** Time series of frequency residuals for MGS occultation 8361M48A. The black line shows original frequency residuals and the grey line shows 100× the frequency residuals, which highlights the positive residuals caused by the ionosphere.

network stations). All these kernels were acquired from http://naif.jpl.nasa.gov.

### 4.2. Time series of frequency residuals

Several frequency residuals from the start and end of the file provided to us were discarded. Some residuals at early times (high altitudes) have unrealistically large values in comparison to adjacent ones, which are probably transient features associated with the start of the experiment. Some residuals at late times (low altitudes) have very low signal power, indicating that here the radio signal was affected by diffraction near the planet's surface. The 2063 frequency residuals that were not discarded by this preprocessing are shown in Fig. 3. The largest positive value of the frequency residuals, 0.06 Hz, corresponds to the ionosphere and the largest negative value of $-10$ Hz corresponds to the near-surface neutral atmosphere. The early frequency residuals correspond to rays that pass far above the atmosphere and ionosphere of Mars. Their standard deviation, 0.04 m Hz, indicates the total noise present in the end-to-end experiment.

### 4.3. Time series of bending angles and impact parameters

The resultant values of the bending angle, $\alpha$, and impact parameter, $a$, are shown in Figs. 4–6. At Mars, which has a thin atmosphere, bending is minimal and the impact parameter $a$ is approximately equal to the distance of closest approach. For reference, note that the mean equatorial radius of Mars is 3396.2 km and, according to the PDS documentation for this occultation, the radial distance to the surface at the location of this occultation is 3376.9 km. Since there are so many different conventions that can be used to convert radial distances into altitudes, we report our results in terms of radial distance for clarity. The largest positive value of the bending angle $\alpha$, $1.3\times10^{-6}$ radians, corresponds to the ionosphere and the largest negative value of $-2\times10^{-4}$ radians corresponds to the near-surface neutral atmosphere. The standard deviation of the high altitude bending angles, $8\times10^{-8}$ radians, indicates the total noise present in the end-to-end experiment. Note that some authors adopt an alternative convention for the sign of the bending angle

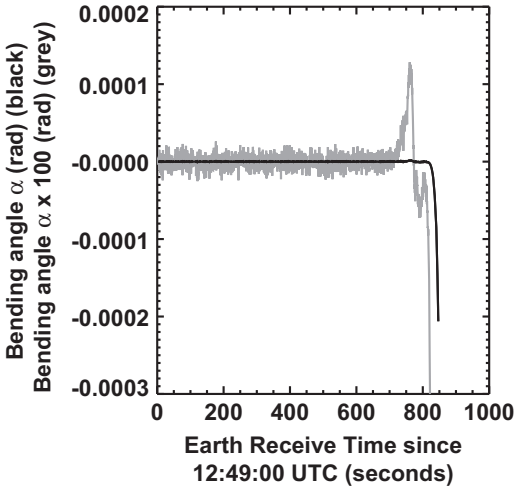


**Fig. 4.** Time series of bending angles $\alpha$ for MGS occultation 8361M48A. The black line shows original bending angles and the grey line shows 100× the bending angles, which highlights the positive bending angles caused by the ionosphere.

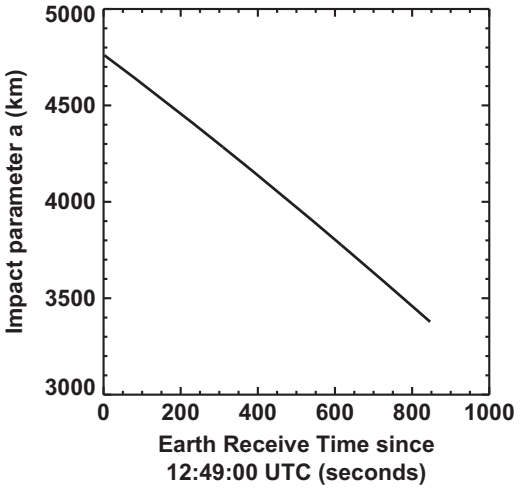


**Fig. 5.** Time series of impact parameters $a$ for MGS occultation 8361M48A.

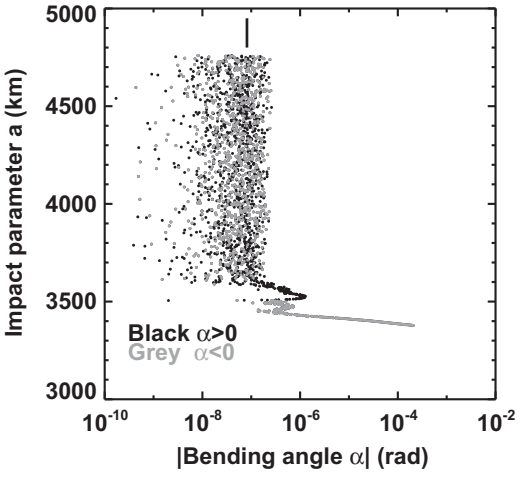


**Fig. 6.** Dependence of bending angle $\alpha$ on impact parameter $a$ for MGS occultation 8361M48A. The absolute magnitude of each value of $\alpha$ is plotted, with black points indicating $\alpha>0$ (the ionosphere) and grey points indicating $\alpha<0$ (the neutral atmosphere). The salt-and-pepper values of $\alpha$ at high altitudes are caused by instrumental noise. The vertical line above the data points shows the standard deviation of the high altitude bending angles, $8\times10^{-8}$ radians, and indicates the smallest measurable bending angle.

and have positive bending angles in the neutral atmosphere (e.g. Ahmad and Tyler, 1998; Hinson et al., 1999; Withers, 2010).

### 4.4. Refractivity profile

The dependence of the refractive index, $\mu$, on radial distance, $R$, can be obtained from the dependence of bending angle, $\alpha$, on impact parameter, $a$, as described in Fjeldbo et al. (1971) and Withers (2010). As previously stated, the point of closest approach of the radio signal transmitted at time $t_A$ to the target object $P$ is $\underline{x}_O$, the time at which this radio signal is at this position is $t_O$, and the two asymptotes of this ray path intersect at position $\underline{x}_X$. The closest approach distance is $|\underline{x}_O(t_O)-\underline{x}_P(t_O)|$, which we now label as $R(t_O)=R_O$. As shown in Appendix C of Fjeldbo et al. (1971), the value of $\mu$ at $R=R_O$ satisfies

$$\pi \ln \mu(R_O) = \int_{a=a_O}^{a=\infty} \ln\left\{\frac{a}{a_O}+\left[\left(\frac{a}{a_O}\right)^2-1\right]^{1/2}\right\}\frac{d\alpha}{da}da \tag{20}$$

where $a_O$ is $a(t_O)$. The integral relationship in Eq. (20) is an example of an Abel transform. Note that the upper boundary of this integral occurs at $a=\infty$, whereas the available data do not extend that far. Also, from Bouguer's rule (Born and Wolf, 1959; Fjeldbo et al., 1971; Kursinski et al., 2000), the value of $R_O$ satisfies

$$R_O = \frac{a_O}{\mu(R_O)} \tag{21}$$

The value of $\mu$ at $R=R_O$ can be found for any $R_O$ using the derived values of $\alpha$ and $a$, thereby yielding the function $\mu(R)$.

Fig. 7 shows how refractivity, $\nu=\mu-1$, depends on the radial distance, $R$. In this instance, the time resolution of 0.4 s in the frequency residuals is equivalent to an altitude resolution of 0.6–1.2 km. Refractivity is positive in the neutral atmosphere ($\mu>1$) and negative in the ionosphere ($\mu<1$). Also shown in Fig. 7 are refractivities associated with the archived profiles. The refractivities are not archived at the PDS; instead, they were provided to us by Dave Hinson. Figs. 8 and 9 illustrate the differences between the derived and archived refractivities. Above 3420 km, the difference has a mean value of $8.6\times10^{-11}$ and a standard deviation of $4.4\times10^{-10}$. Below 3420 km, the refractivities differ by less than 0.5%. In the following discussion, we assume that the refractivity is

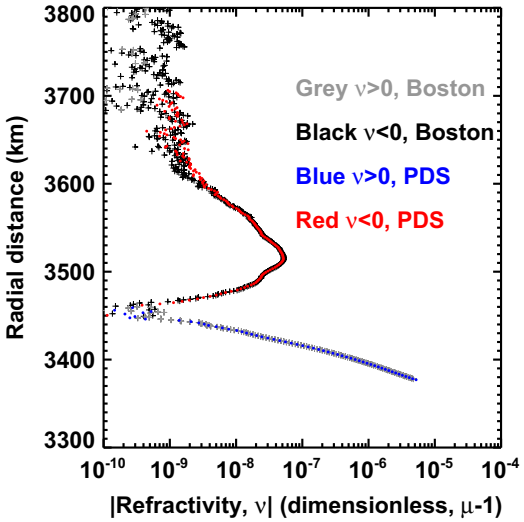


**Fig. 7.** Dependence of refractivity $\nu$ on radial distance $R$ for MGS occultation 8361M48A. The absolute magnitude of each value of $\nu$ is plotted, with black crosses indicating $\nu<0$ (the ionosphere) and grey crosses indicating $\nu>0$ (the neutral atmosphere). Also plotted are refractivities associated with the archived profiles, with red points indicating $\nu<0$ and blue points indicating $\nu>0$. (For interpretation of the references to color in this figure caption, the reader is referred to the web version of this paper.)

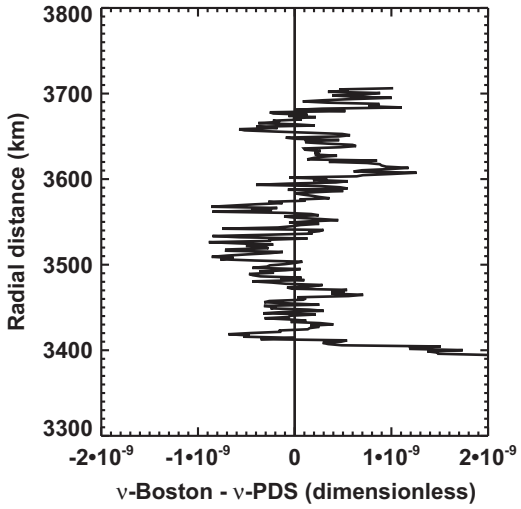


**Fig. 8.** Absolute difference between derived and archived refractivities for MGS occultation 8361M48A as a function of radial distance $R$. This emphasizes the ionospheric results as the absolute difference becomes relatively large at low altitudes.

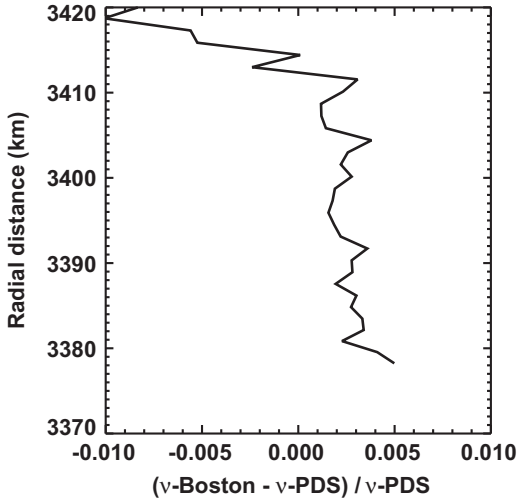


**Fig. 9.** Relative difference between derived and archived refractivities for MGS occultation 8361M48A as a function of radial distance $R$, with emphasis on the low altitudes neglected by Fig. 8.

entirely attributable to the neutral atmosphere at $R<3450$ km and to the ionosphere at $R>3460$ km (Withers, 2010). At high altitudes the neutral density is not sufficient to affect the refractivity appreciably and at low altitudes the plasma density is not sufficient to affect the refractivity appreciably.

### 4.5. Ionospheric and atmospheric properties

Vertical profiles of the neutral and plasma number densities follow directly from the refractive index, $\mu$ (Withers, 2010). The total refractivity of the atmosphere, $\nu=\mu-1$, is the sum of the refractivity of the ionosphere, $\nu_e$, and the refractivity of the neutral atmosphere, $\nu_n$ (Eshleman, 1973)

$$\nu = \nu_e + \nu_n \tag{22}$$

For typical radio occultation experiments in planetary ionospheres, $\mu_e$ satisfies

$$\mu_e - 1 = \nu_e = -\frac{N_e e^2}{8\pi^2 m_e \epsilon_0 f^2} \tag{23}$$

Thus $N_e(r)$ can be determined from $\nu_e(r)$. Note that refractivity of the ionosphere is frequency dependent.

The refractive index of the neutral atmosphere, $\mu_n$, satisfies

$$\mu_n - 1 = \nu_n = \sum \kappa_i n_{n,i} \quad (24)$$

where $\kappa_i$ is the refractive volume of constituent $i$ and $n_{n,i}$ is the number density of constituent $i$ (Eshleman, 1973). The contributions of aerosols and condensates, such as dust or clouds, to the refractivity of the neutral atmosphere can be ignored because they do not affect the propagation of electromagnetic waves at typical radio occultation frequencies. A mean refractive volume, $\kappa$, can be defined based on the known chemical composition of the atmosphere such that

$$\nu_n = \kappa n_n \quad (25)$$

where $n_n$ is the total neutral number density. Hence $n_n(r)$ can be found from $\nu_n(r)$. Note that refractivity of the neutral atmosphere is not frequency dependent.

Fig. 10A shows the electron density profile, which was obtained from the refractivity profile using an assumed radio frequency of 8.423 GHz (Hinson et al., 1999; Withers, 2010). Fig. 10B illustrates the differences between the derived and archived electron density profiles. The mean and the standard deviation of the differences are $2 \times 10^8$ m$^{-3}$ and $7 \times 10^8$ m$^{-3}$, respectively. The average of the uncertainties in the archived electron density values is $1.9 \times 10^9$ m$^{-3}$, which indicates that the differences between the derived and archived electron density profiles are not statistically significant.

Fig. 11A shows the neutral number density profile, $n_n(R)$, which was obtained from the refractivity profile using $\kappa = 1.804 \times 10^{-29}$ m$^3$ for the refractive volume of the atmosphere (Hinson et al., 1999). The inferred neutral number density is dominated by the experimental noise above 3440 km, so the profiles of neutral atmospheric properties are truncated at 3440 km. Even so, our derived neutral number densities extend to higher altitudes than the archived values, presumably reflecting conservative choices by the MGS radio science team regarding archiving policies. Fig. 11B illustrates the differences between the derived and archived neutral number density profiles. The derived number densities are systematically larger than the archived number densities by up to 0.4%, and the difference diminishes as altitude increases. These differences could arise from choices regarding numerical integration techniques. The Abel transform generates results that are very sensitive to its implementation and it can also readily introduce a systematic offset into its results. Different versions of generic SPICE kernels could also cause differences.

The mass density profile, $\rho(R) = mn_n(R)$, where the mean molecular mass $m = 7.221 \times 10^{-26}$ kg, independent of altitude (Hinson et al., 1999). The mass density profile is shown in Fig. 11C. We are unable to compare our mass density profile to the archived mass density profile, since the archived neutral atmospheric properties do not include mass densities. In order to maintain consistency throughout Fig. 11, we therefore estimated an "archived" mass density profile from the archived neutral number density profile using $m = 7.221 \times 10^{-26}$ kg. This is shown in Fig. 11C as a reference. Fig. 11D is thus identical to Fig. 11B.

The pressure profile, $p(R)$, can be found from $\rho(R)$, the known gravitational field, and an upper boundary condition via the equation of hydrostatic equilibrium. Multiple models exist for the gravitational field of Mars, which varies with latitude and longitude. In order to ensure that our assumptions were consistent with those of the MGS team, we inferred the gravitational acceleration, $g$, actually used by the MGS team from $g = -dp/dz \times 1/\rho$ via the archived densities and pressure gradients. The result was consistent with $g = GM/R^2$, where $GM = 4.26 \times 10^{13}$ m$^3$ s$^{-2}$. The upper boundary condition can be an assumed temperature or pressure. It can also be obtained from the scale height of $n_n(R)$ under certain reasonable assumptions (Withers et al., 2003b; Tellmann et al., 2009). Here we find the scale height, $H$, for neutral number densities between 3430 km and 3440 km, which equals 6.2 km, and assume $p(3440\text{ km}) = \rho(3440\text{ km}) \times g(3440\text{ km}) \times H$. Errors in the upper boundary condition have minimal effect on the derived pressures at altitudes more than several scale heights below the upper boundary (Withers et al., 2003b). Fig. 11E shows the neutral pressure profile and Fig. 11F illustrates the differences between the derived and archived neutral pressure profiles. As with the neutral number densities and for the same reason, our derived pressures extend to higher altitudes than the archived values. The large differences between derived and archived pressures at high altitudes is hence simply the outcome of slight inconsistencies in upper boundary conditions, which is most visible as the offset in temperatures at the top of the archived profile. The effects of imposed upper boundary conditions diminish as altitude decreases and the difference

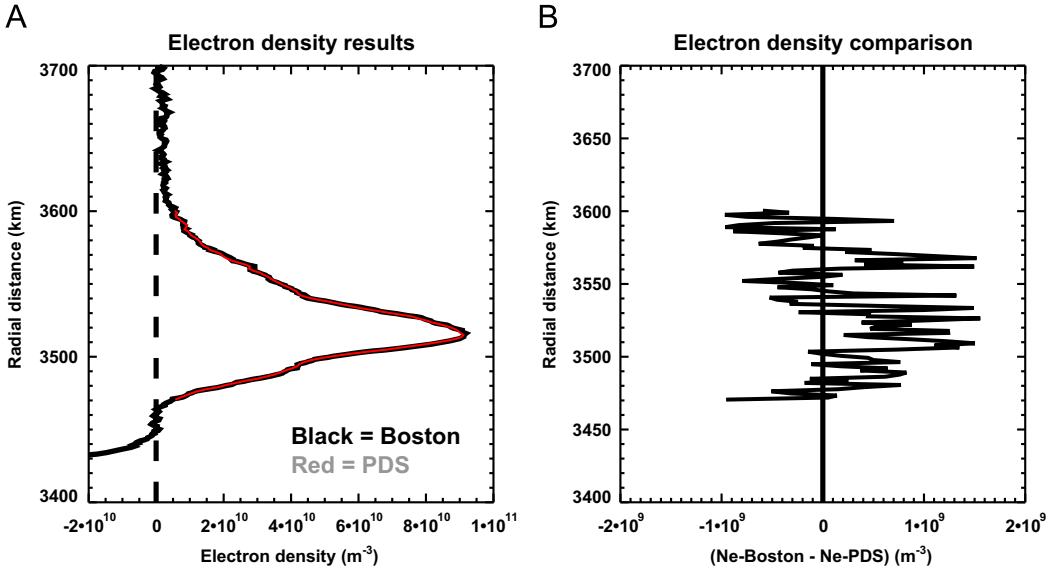


**Fig. 10.** (A) Derived profile of ionospheric electron density for MGS occultation 8361M48A (black). Also shown is the corresponding archived profile (red). (B) Comparison between the two profiles shown in Panel A, where Ne is the electron density. (For interpretation of the references to color in this figure caption, the reader is referred to the web version of this paper.)

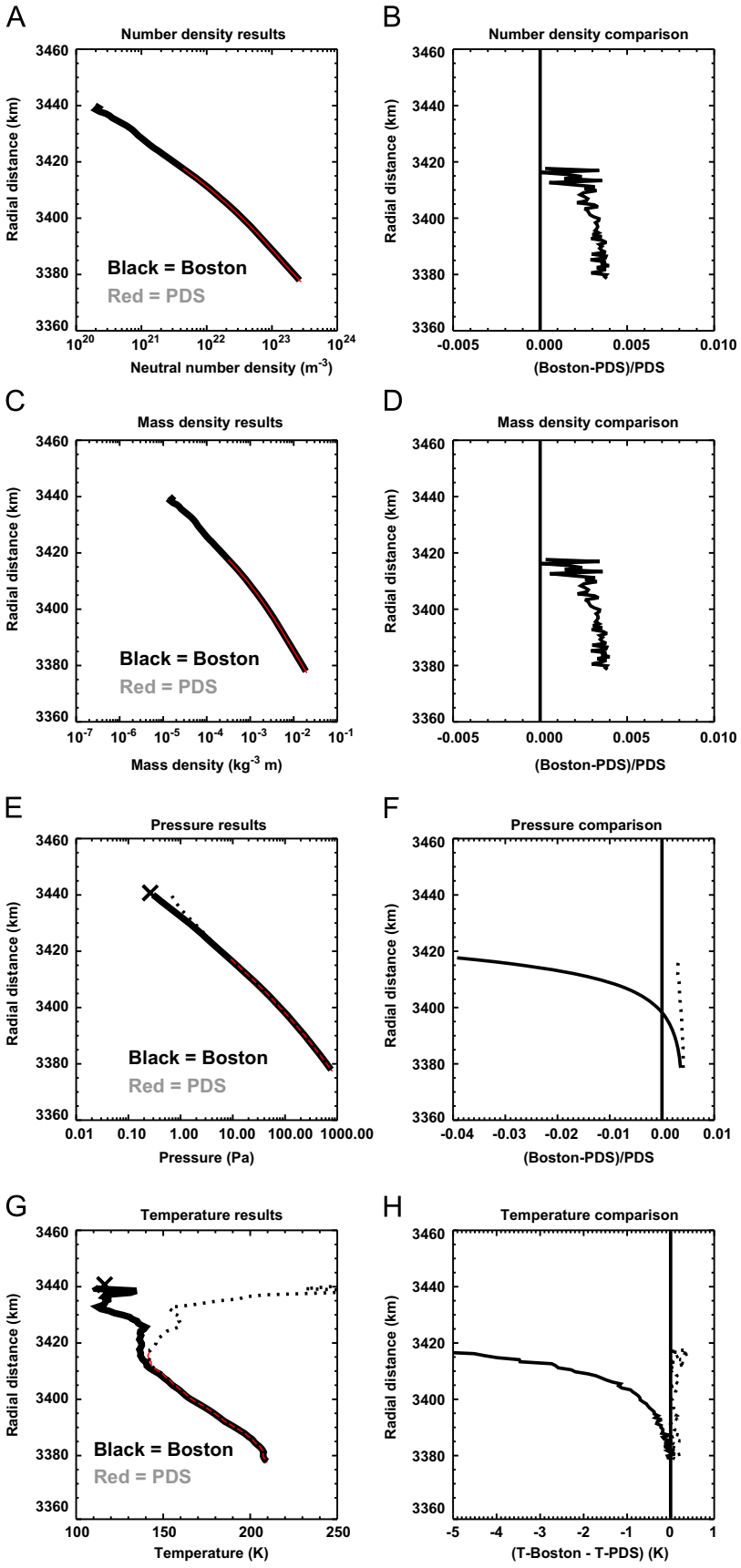


**Fig. 11.** (A) Derived profile of neutral number density for MGS occultation 8361M48A (black). Also shown is the corresponding archived profile (red). (B) Comparison between the two profiles shown in Panel A. Panels C and D are as panels A and B, but for neutral mass density. Panels E and F are as panels A and B, but for neutral pressure. Panels G and H are as panels A and B, but for neutral temperature. The *X* at 3440 km in Panels E and G highlights the imposed upper boundary conditions. Dotted lines in Panels E–H show profiles that use alternate upper boundary conditions, as discussed in the text. (For interpretation of the references to color in this figure caption, the reader is referred to the web version of this paper.)

between derived and archived pressures levels off at 0.3–0.4%, which is consistent with the differences in the neutral number density in Fig. 11B. The effects of the upper boundary condition are illustrated by an alternate neutral pressure profile that was obtained using a different upper condition, one chosen to improve agreement with the PDS profile. This alternate profile is shown by the dotted lines in Fig. 11Eand F. The difference between alternate and archived pressures is everywhere less than 0.4%, again consistent with the differences in the neutral number density in Fig. 11B.

The temperature profile, $T(R)$, can be found from $p(R)$, the atmospheric composition and either $n_n(R)$ or $\rho(R)$ via an equation of state, such as the ideal gas law. Errors in the upper boundary condition of the equation of hydrostatic equilibrium have minimal effect on the derived temperatures at altitudes more than several scale heights below the upper boundary (Withers et al., 2003b). Here we used the ideal gas law $p=\rho kT/m$, where $k$ is Boltzmann's constant, with our assumed mean molecular mass. Fig. 11G shows the neutral temperature profile and Fig. 11H illustrates the differences between the derived and archived neutral temperature profiles. Differences are noticeable at high altitudes due to slight inconsistencies in assumed upper boundary conditions, but are less than 0.1 K at the lowest altitudes. The effects of the upper boundary condition are illustrated by an alternate neutral temperature profile that was obtained using the alternate neutral pressure profile shown in Fig. 11E. This alternate profile is shown by the dotted lines in Fig. 11G and H. The difference between alternate and archived temperatures is everywhere less than 0.5 K and the mean difference is 0.1 K.

## 5. Limitations

There are many types of radio occultation experiments and the methods provided here do not apply to all of them. Our methods assume a (1) one-way (2) single frequency experiment with a transmitter that has a (3) stable frequency source and a target object whose atmosphere and ionosphere can be assumed to be (4) spherically symmetric, for which (5) frequency residuals have already been obtained from raw data. Each numbered point is responsible for limitations in our methods, as enumerated below.

(1) In two-way experiments such as those performed by Mars Express, the radio signal propagates through the atmosphere/ionosphere twice, with the ray passing through different regions on the uplink and downlink legs (Pätzold et al., 2004). Separation of the refraction experienced in the neutral atmosphere on the two legs is challenging and beyond the scope of the current work. However, the refraction experienced in the ionosphere, which is frequency dependent, is readily separated (Pätzold et al., 2004). (2) In multi-frequency experiments such as those performed by Cassini, comparison of frequency residuals at different frequencies can isolate ionospheric refraction and eliminate many sources of error (Kliore et al., 2004; Pätzold et al., 2004; Häusler et al., 2006). Of course, a multi-frequency downlink experiment can also be considered as a set of independent single frequency downlink experiments. (3) If the spacecraft does not have a stable frequency source, such as an ultrastable oscillator, then acceptable measurement accuracy requires that the spacecraft merely serve as a transponder for a signal transmitted and received elsewhere, most likely at a ground station equipped with a stable frequency source (Pätzold et al., 2004). Consequently, the occultation must be a two-way occultation. (4) If the atmosphere and ionosphere of the target object cannot be assumed to be spherically symmetric, then gradients of refractivity will exist perpendicular to the $r-z$ plane in Fig. 1 that contains the transmitter, receiver, and target object, and thus the radio signal will travel outside this plane (see Eq. (1)). Obviously atmospheres and ionospheres are not perfectly spherically symmetric as their properties routinely vary with latitude, local time, or solar zenith angle. However, as long as their properties do not vary appreciably with horizontal distance over a lengthscale $\sqrt{2RL}$, where $R$ is the planetary radius and $L$ is the vertical lengthscale for changes in density (Hinson et al., 1999), then the assumption of spherical symmetry is adequate. Our methods will not perform well at the oblate giant planets (Kliore et al., 1974, 1975; Hubbard et al., 1975; Lindal, 1992). Nevertheless, many atmospheres and ionospheres in the solar system can be assumed to be spherically symmetric for the purpose of occultation analysis, including those of the Sun, Mercury, Venus, Earth, the Moon, Mars, the four Galilean satellites, Titan, Enceladus, and Triton. (5) This work does not address how to produce frequency residuals from raw data, so is only immediately applicable in cases where frequency residuals are archived. Frequency residuals from Venus Express and Mars Express are known to be available at archives, though the methods developed in this work are not able to tackle the two-way occultations of Mars Express, and it is possible that frequency residuals from other missions exist in archives we have yet to discover. Although Eq. (3) is central to finding the predicted “direct” received frequency, there are a great many additional subtleties that must be considered and we intend to address this topic in future work.

Readers considering using the methods outlined in this work should also bear in mind that (A) even archived frequency residuals may contain offsets or drifts due to incomplete knowledge of either the spacecraft trajectory or other contributions to the Doppler shift, which will particularly impact results in the relatively unrefractive ionosphere (elimination of these potential ionospheric problems in a multi-frequency occultation is one major factor that favors this type of experiment). (B) Noise and other effects can cause the bending angle and impact parameter not to be monotonic functions of time, yet the Abel transform from bending angle and impact parameter to refractivity and radial distance requires the series of impact parameters to vary monotonically. (C) Diffraction effects near the surfaces of solid target objects and multipath propagation effects can lead to erroneous results if they are not corrected for. Back-propagation analysis methods exist that can handle diffraction and multipath effects (Karayel and Hinson, 1997; Marouf et al., 1986). As these methods go beyond the limitations of ray-based geometrical optics, they permit sub-Fresnel scale spatial resolution.

Despite the limitations of the methods described here, and despite the fact that the state-of-the-art tools used by radio science teams at JPL, Stanford, and Cologne are unquestionably more sophisticated than those described in this work, this work still has value. Specifically, this work makes a functional tool for investigating and analyzing radio occultation data available to all.

## 6. Discussion and conclusions

Raw radio occultation data are hard to process into scientifically useful data products and the necessary skills are not widespread. Here we have provided detailed instructions and accompanying software for one critical aspect of radio occultation data processing: how to obtain a series of bending angles $\alpha$ as a function of the ray impact parameter $a$ from a time series of frequency residuals. The software also performs the next step of converting bending angles and impact parameters into vertical profiles of ionospheric electron density, neutral atmospheric number density, mass density, pressure, and temperature, all quantities that are scientifically useful. It is critically important to work in a frame centered on and moving with the target object, since only in that frame does a radio ray encounter a spherically

symmetric atmosphere, and to account for light travel times throughout the analysis.

However, these specific methods are limited. As currently developed, they are valid only for a one-way, single frequency, downlink experiment with a transmitter that has a stable frequency source and a target object whose atmosphere and ionosphere can be assumed to be spherically symmetric. These methods cannot be immediately applied to two-way radio occultations, such as Mars Express, in which a radio signal propagates twice through the atmosphere and ionosphere of the target object or to giant planet occultations, where the atmosphere and ionosphere of the target object are significantly oblate. They also require that raw radio occultation data have been pre-processed to the frequency residuals stage. Yet they provide the wider community with some much-needed abilities to work with radio occultation data and they are a necessary foundation for anticipated development into a more general tool.

These methods were demonstrated successfully on data from a Mars Global Surveyor occultation at Mars. The differences between the derived and archived electron densities are only about one-third of the uncertainty in the archived electron densities, a difference which is equivalent to less than 0.5% of the subsolar peak electron density. If the upper boundary condition imposed for the equation of hydrostatic equilibrium is guided by the archived neutral profiles, then derived and archived neutral profiles differ by less than 0.4% (densities and pressures) or 0.5 K (temperatures). These results are close enough to demonstrate that our processing programs are working well. The remaining improvements that are required are likely incremental, rather than substantial. These differences may be caused by differences in the implementation of the Abel transform used to derive refractive index or in the generic SPICE kernels. The uncertainties in our results have not been quantified yet. The uncertainty in the frequency residuals, 0.04 m Hz, is readily calculated, but the propagation of these uncertainties through the Abel transform and other processing steps is sufficiently non-trivial to merit careful attention in a separate manuscript (e.g., Lipa and Tyler, 1979).

Computer programs that implement the data processing methods outlined here using the IDL programming language accompany this paper. We encourage readers to inspect them and run them using the examples provided and other recordings of time series of frequency residuals. The tools provided here are sufficiently powerful that readers can recreate atmospheric and ionospheric profiles for old missions whose final profiles are not widely available. We also hope that readers will improve these programs and make their improvements publicly available. This will enhance the quality of any recreated atmospheric and ionospheric profiles and further improve the radio occultation data processing skills of the broad planetary science community.

## Acknowledgments

We thank the Mars Express and Venus Express radio science teams for helpful discussions and Dave Hinson for MGS data products and extremely valuable comments. This paper was immeasurably improved by comments from Mike Bird, Silvia Tellmann, and an anonymous reviewer.

## Appendix A. Non-relativistic frequency residual

If relativistic terms of order $U/c^2$ or $(v/c)^2$ and higher can be neglected, then Eq. (4) becomes

$$\frac{\Delta f(t_B)}{f_A(t_A)} = \frac{\underline{v}_A(t_A)}{c} \cdot (\underline{\hat{n}}_{A,Occ}(t_A) - \underline{\hat{n}}_{A,Direct}(t_A)) - \frac{\underline{v}_B(t_B)}{c} \cdot (\underline{\hat{n}}_{B,Occ}(t_B) - \underline{\hat{n}}_{B,Direct}(t_B)) \quad (26)$$

This emphasizes that the root causes of the frequency residual are the differences in ray propagation directions at the transmitter and receiver. For the MGS-like case in which the target object $P$ is much closer to the transmitter $A$ than to the receiver $B$, $\delta_X \ll \beta_X$ and $|\underline{\hat{n}}_{B,Occ}(t_B) - \underline{\hat{n}}_{B,Direct}(t_B)| \ll |\underline{\hat{n}}_{A,Occ}(t_A) - \underline{\hat{n}}_{A,Direct}(t_A)|$.

Hence Eq. (26) is approximately

$$\frac{\Delta f(t_B)}{f_A(t_A)} = \frac{\underline{v}_A(t_A)}{c} \cdot (\underline{\hat{n}}_{A,Occ}(t_A) - \underline{\hat{n}}_{A,Direct}(t_A)) \quad (27)$$

Since $\delta_X \ll \beta_X$ means that $\beta_X = \alpha$, we can write $\underline{\hat{n}}_{A,Occ}(t_A)$ in terms of $\underline{\hat{n}}_{A,Direct}(t_A)$ and $\alpha$

$$\underline{\hat{n}}_{A,Occ}(t_A) = \underline{\hat{n}}_{A,Direct}(t_A) \cos\ \alpha + (\underline{\hat{n}}_{A,Direct}(t_A) \times \underline{\hat{n}}(t_O)) \sin\ \alpha \quad (28)$$

where $\underline{\hat{n}}(t_O)$ is one of the unit vectors defining our frame (Eq. (2)). Substituting this into Eq. (27) leads to

$$\frac{\Delta f(t_B)}{f_A(t_A)} = \frac{\underline{v}_A(t_A)}{c} \times (\underline{\hat{n}}_{A,Direct}(t_A)(\cos\ \alpha - 1) + (\underline{\hat{n}}_{A,Direct}(t_A) \times \underline{\hat{n}}(t_O)) \sin\ \alpha) \quad (29)$$

For small bending angles, as long as $\underline{v}_A(t_A)$ is not nearly parallel with $\underline{\hat{n}}_{A,Direct}(t_A)$, this reduces to

$$\frac{\Delta f(t_B)}{f_A(t_A)} = \frac{\underline{v}_A(t_A)}{c} \cdot (\underline{\hat{n}}_{A,Direct}(t_A) \times \underline{\hat{n}}(t_O))\alpha \quad (30)$$

That is, $\Delta f = v_\perp \alpha/\lambda$, where $v_\perp$ is the component of the transmitter's velocity relative to the target object that is in the transmitter-target object-receiver plane and perpendicular to the line of sight between the transmitter $A$ and the receiver $B$. It is counterintuitive that a difference in frequency connected with a Doppler shift is controlled by the velocity component perpendicular to, not parallel to, the line of sight.

## Appendix B. Supplementary data

Supplementary data associated with this article can be found in the online version at http://dx.doi.org/10.1016/j.pss.2014.06.011.

## References

Ahmad, B., Tyler, G.L., 1998. The two-dimensional resolution kernel associated with retrieval of ionospheric and atmospheric refractivity profiles by Abelian inversion of radio occultation phase data. Radio Sci. 33, 129–142.

Anthes, R.A., Bernhardt, P.A., Chen, Y., Cucurull, L., Dymond, K.F., Ector, D., Healy, S.B., Ho, S.-P., Hunt, D.C., Kuo, Y.-H., Liu, H., Manning, K., McCormick, C., Meehan, T.K., Randel, W.J., Rocken, C., Schreiner, W.S., Sokolovskiy, S.V., Syndergaard, S., Thompson, D.C., Trenberth, K.E., Wee, T.-K., Yen, N.L., Zeng, Z., 2008. The COSMIC/FORMOSAT-3 mission: early results. Bull. Am. Met. Soc. 89, 313–333.

Born, M., Wolf, E., 1959. Principles of Optics. Pergamon Press, London.

Eshleman, V.R., 1973. The radio occultation method for the study of planetary atmospheres. Planet. Space Sci. 21, 1521–1531.

Fjeldbo, G., Kliore, A.J., Eshleman, V.R., 1971. The neutral atmosphere of Venus as studied with the Mariner V radio occultation experiments. Astron. J. 76, 123–140.

Häusler, B., Pätzold, M., Tyler, G.L., Barriot, J., Bird, M.K., Dehant, V., Hinson, D., Simpson, R.A., Treumann, R.A., Eidel, W., Mattei, R., Rosenblatt, P., Remus, S., Selle, J., 2007. Venus Atmospheric, Ionospheric, Surface and Interplanetary Radio-Wave Propagation Studies with the VeRA Radio-Science Experiment. ESA SP-1295: Venus Express, pp. 1–30. Available from: ⟨http://sci.esa.int/venus-express/41535-vera-radio-science-experiment/⟩.

Häusler, B., Pätzold, M., Tyler, G.L., Simpson, R.A., Bird, M.K., Dehant, V., Barriot, J., Eidel, W., Mattei, R., Remus, S., Selle, J., Tellmann, S., Imamura, T., 2006. Radio science investigations by VeRa onboard the Venus Express spacecraft. Planet. Space Sci. 54, 1315–1335.

Hinson, D.P., Simpson, R.A., Twicken, J.D., Tyler, G.L., Flasar, F.M., 1999. Initial results from radio occultation measurements with Mars Global Surveyor. J. Geophys. Res. 104, 26997–27012.

Hu, X., Wu, X.-C., Gong, X.-Y., Wang, X., Xu, Q.-C., 2010. An emulation research on the radio occultation exploration of Martian ionosphere. Chinese Astron. Astrophys. 34 (January), 100–112.

Hubbard, W.B., Hunten, D.M., Kliore, A., 1975. Effect of the Jovian oblateness on Pioneer 10/11 radio occultations. Geophys. Res. Lett. 2, 265–268.

Imamura, T., Nabatov, A., Mochizuki, N., Iwata, T., Hanada, H., Matsumoto, K., Noda, H., Kono, Y., Liu, Q., Futaana, Y., Ando, H., Yamamoto, Z., Oyama, K.-I., Saito, A., 2012. Radio occultation measurement of the electron density near the lunar surface using a subsatellite on the SELENE mission. J. Geophys. Res. 117, A06303, http://dx.doi.org/10.1029/2011JA017293.

Imamura, T., Toda, T., Tomiki, A., Hirahara, D., Hayashiyama, T., Mochizuki, N., Yamamoto, Z.-I., Abe, T., Iwata, T., Noda, H., Futaana, Y., Ando, H., Häusler, B., Pätzold, M., Nabatov, A., 2011. Radio occultation experiment of the Venus atmosphere and ionosphere with the Venus orbiter Akatsuki. Earth Planets Space 63, 493–501.

Karayel, E.T., Hinson, D.P., 1997. Sub-Fresnel-scale vertical resolution in atmospheric profiles from radio occultation. Radio Sci. 32, 411–424.

Kliore, A., Cain, D.L., Fjeldbo, G., Seidel, B.L., Rasool, S.I., 1974. Preliminary results on the atmospheres of Io and Jupiter from the Pioneer 10 S-band occultation experiment. Science 183, 323–324.

Kliore, A., Cain, D.L., Levy, G.S., Eshleman, V.R., Fjeldbo, G., Drake, F.D., 1965. Occultation experiment: results of the first direct measurement of Mars's atmosphere and ionosphere. Science 149, 1243–1248.

Kliore, A., Fjeldbo, G., Seidel, B.L., Sesplaukis, T.T., Sweetnam, D.W., Woiceshyn, P.M., 1975. Atmosphere of Jupiter from the Pioneer 11 S-band occultation experiment—preliminary results. Science 188, 474–476.

Kliore, A.J., Anderson, J.D., Armstrong, J.W., Asmar, S.W., Hamilton, C.L., Rappaport, N.J., Wahlquist, H.D., Ambrosini, R., Flasar, F.M., French, R.G., Iess, L., Marouf, E. A., Nagy, A.F., 2004. Cassini radio science. Space Sci. Rev. 115, 1–70.

Kursinski, E.R., Hajj, G.-A., Leroy, S.S., Herman, B., 2000. The GPS radio occultation technique. Terr. Atmos. Ocean. Sci. 11, 53–114.

Kursinski, E.R., Hajj, G.A., Schofield, J.T., Linfield, R.P., Hardy, K.R., 1997. Observing Earth's atmosphere with radio occultation measurements using the Global Positioning System. J. Geophys. Res. 102, 23429–23465.

Lindal, G.F., 1992. The atmosphere of Neptune—an analysis of radio occultation data acquired with Voyager 2. Astron. J. 103, 967–982.

Lipa, B., Tyler, G.L., 1979. Statistical and computational uncertainties in atmospheric profiles from radio occultation—Mariner 10 at Venus. Icarus 39, 192–208.

Marouf, E.A., Tyler, G.L., Rosen, P.A., 1986. Profiling Saturn's rings by radio occultation. Icarus 68, 120–166.

Nicholson, P.D., Muhleman, D.O., 1978. Independent radio-occultation studies of Venus' atmospheres. Icarus 33, 89–101.

Noguchi, K., Imamura, T., Oyama, K.-I., Nabatov, A.S., 2002. Radio-occultation projects in space programs of Japan. Radio Sci. Bull. 303, 27–31.

Oyama, K.-I., Nabatov, A.S., Savich, N.A., Yamamoto, Z., Imamura, T., Ichikawa, T., Noguchi, K., 2001. First test of the NOZOMI radio science system in actual space flight. Adv. Space Res. 27, 1847–1850.

Pätzold, M., Häusler, B., Aksnes, K., Anderson, J.D., Asmar, S.W., Barriot, J.-P., Bird, M.K., Boehnhardt, H., Eidel, W., Grün, E., Ip, W.H., Marouf, E., Morley, T., Neubauer, F.M., Rickman, H., Thomas, N., Tsurutani, B.T., Wallis, M.K., Wickramasinghe, N.C., Mysen, E., Olson, O., Remus, S., Tellmann, S., Andert, T., Carone, L., Fels, M., Stanzel, C., Audenrieth-Kersten, I., Gahr, A., Müller, A.-L., Stupar, D., Walter, C., 2007. Rosetta Radio Science Investigations (RSI). Space Sci. Rev. 128, 599–627.

Pätzold, M., Neubauer, F.M., Carone, L., Hagermann, A., Stanzel, C., Häusler, B., Remus, S., Selle, J., Hagl, D., Hinson, D.P., Simpson, R.A., Tyler, G.L., Asmar, S.W., Axford, W.I., Hagfors, T., Barriot, J.-P., Cerisier, J.-C., Imamura, T., Oyama, K.-I., Janle, P., Kirchengast, G., Dehant, V., 2004. MaRS: Mars Express Orbiter Radio Science. ESA SP-1240: Mars Express: the Scientific Payload, pp. 141–163. Available from: ⟨http://sci.esa.int/science-e/www/object/index.cfm?fobjectid=34885⟩.

Phinney, R.A., Anderson, D.L., 1968. On the radio occultation method for studying planetary atmospheres. J. Geophys. Res. 73, 1819–1827.

Soffel, M.H., 1989. Relativity in Astrometry, Celestial Mechanics and Geodesy. Springer-Verlag, New York.

Tellmann, S., Pätzold, M., Häusler, B., Bird, M.K., Tyler, G.L., 2009. Structure of the Venus neutral atmosphere as observed by the Radio Science experiment VeRa on Venus Express. J. Geophys. Res. 114, E00B36, http://dx.doi.org/10.1029/2008JE003204.

Withers, P., 2010. Prediction of uncertainties in atmospheric properties measured by radio occultation experiments. Adv. Space Res. 46, 58–73.

Withers, P., Bougher, S.W., Keating, G.M., 2003a. The effects of topographically-controlled thermal tides in the martian upper atmosphere as seen by the MGS accelerometer. Icarus 164, 14–32.

Withers, P., Towner, M.C., Hathi, B., Zarnecki, J.C., 2003b. Analysis of entry accelerometer data: a case study of Mars Pathfinder. Planet. Space Sci. 51, 541–561.

Yakovlev, O.I., 2002. Space Radio Science. Taylor and Francis, New York.